Combining Satellite Microwave Radiometer and Radar Observations to Estimate Atmospheric Latent Heating Profiles

by

Mircea Grecu[1], William S. Olson[2], Chung-Lin Shie[1], Tristan S. L'Ecuyer[3], and Wei-Kuo Tao[4]

[1] Goddard Earth Sciences and Technology Center, University of Maryland Baltimore County, Baltimore, MD

[2] Joint Center for Earth Systems Technology, University of Maryland Baltimore County, Baltimore, MD

[3] Department of Atmospheric Science, Colorado State University, Fort Collins, CO

[4] Laboratory for Atmospheres, NASA/Goddard Space Flight Center, Greenbelt, MD

submitted to *Journal of Climate*

December 31, 2008

Corresponding author address: Dr. Mircea Grecu, NASA/Goddard Space Flight Center, Code 613.1, Greenbelt, MD 20771 Mircea.Grecu-1@nasa.gov

Abstract

In this study, satellite passive microwave sensor observations from the TRMM Microwave Imager (TMI) are utilized to make estimates of latent + eddy sensible heating rates (Q_1-Q_R) in regions of precipitation. The TMI heating algorithm (TRAIN) is calibrated, or "trained" using relatively accurate estimates of heating based upon spaceborne Precipitation Radar (PR) observations collocated with the TMI observations over a one-month period. The heating estimation technique is based upon a previously described Bayesian methodology, but with improvements in supporting cloud-resolving model simulations, an adjustment of precipitation echo tops to compensate for model biases, and a separate scaling of convective and stratiform heating components that leads to an approximate balance between estimated vertically-integrated condensation and surface precipitation.

Estimates of Q_1-Q_R from TMI compare favorably with the PR training estimates and show only modest sensitivity to the cloud-resolving model simulations of heating used to construct the training data. Moreover, the net condensation in the corresponding annual mean satellite latent heating profile is within a few percent of the annual mean surface precipitation rate over the tropical and subtropical oceans where the algorithm is applied. Comparisons of Q_1 produced by combining TMI Q_1-Q_R with independently derived estimates of Q_R show reasonable agreement with rawinsonde-based analyses of Q_1 from two field campaigns, although the satellite estimates exhibit heating profile structure with sharper and more intense heating peaks than the rawinsonde estimates.

1. Introduction

The latent heat released or consumed during phase changes of water substance is a major component of the atmospheric energy budget, and one that dominates other diabatic processes in the deep tropics; see Newell (1969); Schaack et al. (1990). Latent heating is also responsible for the creation of available potential energy, one mechanism by which convective clouds can interact with the larger-scale atmospheric circulations of their environment (Nitta 1970, 1972; Yanai et al. 2000), and the atmospheric response to heating is sensitive to its vertical distribution; e.g. Hartmann et al. (1984), Lau and Peng (1987), Puri (1987), Valdes and Hoskins (1989), Mapes and Houze (1995), Schumacher et al. (2004). Considering either diagnostics of the atmospheric energy budget or cloud-environment interactions, knowledge of the four-dimensional distribution of latent heating on a global basis is of value.

Given the interest in atmospheric latent heating distributions from these different perspectives, several methods for estimating latent heating from satellite observations have been developed. Tao et al. (1990) and Smith et al. (1994) used satellite estimates of precipitation vertical structure to infer latent heating rates in discrete atmospheric layers, assuming that the net flux of precipitation into or out of a given layer is balanced by microphysical processes under steady state conditions. Tao et al. (1993) later simplified their approach by treating the entire atmospheric column as a single layer, scaling representative convective and stratiform heating profiles from cloud-resolving model simulations by the net convective and stratiform precipitation fluxes, respectively, at the surface. Shige et al. (2004; hereafter SH) expanded upon this technique, extracting precipitation column depth as well as convective-stratiform proportion information from

spaceborne radar observations to further categorize a given vertical profile, and then assigning consistent cloud-resolving model generated heating profiles to each category of precipitation profile. Shige et al. (2007) improved upon their method by subdividing the atmosphere (at the freezing level) in convective regions into two layers and applying a precipitation flux scaling of cloud-model generated profiles in each layer. In an alternative approach, Satoh and Noda (2001) and Katsumata et al. (2009a) applied a steady-state moisture budget to the atmospheric column, and adjusted parameterized profiles of vertical motion to yield profiles of net condensation and latent heating consistent with satellite-observed precipitation.

Although the methods of Tao et al. (1993) and Smith et al. (1994) have been applied to precipitation estimates from satellite passive microwave sensors, the aforementioned studies have primarily emphasized methods that utilize the detailed vertical precipitation structure information available from spaceborne radar to estimate latent heating. In a separate line of investigation, Olson et al. (1999), Olson et al. (2006), and Grecu and Olson (2006; hereafter GO), developed methods that directly interpreted satellite passive microwave signatures in terms of heating vertical structure. The first two of these studies utilized cloud-resolving model simulations to synthesize microwave radiances; the model relationships between radiances and heating profiles were then employed in a Bayesian methodology for inferring heating profiles from satellite microwave sensor observations. These attempts to "train" a passive microwave heating algorithm using only cloud-resolving model simulations resulted in high biases of estimated upper-tropospheric precipitation and heating, due to high biases in the precipitation simulations and synthesized microwave signatures; see Lang et al. (2007). In GO, the high biases in

estimated precipitation and heating profiles were overcome using globally-distributed spaceborne radar profiles of precipitation/heating instead of a limited number of cloud model simulations to train the passive microwave algorithm. However, in the GO study, the estimation of precipitation profiles was emphasized, and only limited comparative data were used to evaluate the estimates of heating vertical structure.

In the present study, the satellite passive microwave remote-sensing method for estimating vertical latent heating profiles that was briefly introduced in GO is revised and analyzed, with emphasis on the evaluation of uncertainties in heating estimates. The estimation method, identified here as TRAIN, relies on two algorithms: the first utilizes cloud-resolving model simulations to interpret features of the vertical profiles of reflectivity measured by spaceborne radar to estimate vertical heating profiles. An algorithm of this kind was shown by Shige et al. (2004, 2007) to produce heating estimates with reasonable accuracy in synthetic data tests and in comparisons to independent rawinsonde-based estimates of heating. However, in order to overcome the limited global sampling by spaceborne radars, heating estimates from the spaceborne radar algorithm are used to train a second algorithm that requires only satellite passive microwave radiometer observations to estimate heating.

Relative to GO, the satellite microwave estimation method is modified to improve the heating diagnosis and clarify the analysis of the estimates: First, only spaceborne radar (Precipitation Radar, or PR) data from the TRMM standard algorithm are used for training, as opposed to the combined radar-microwave algorithm training of GO, in an effort to make to the training algorithm a more independent reference. In addition, although the passive microwave heating algorithm is not solely dependent on cloud-

resolving model simulations for training, as in implementations prior to GO, these simulations still have an impact through the PR training algorithm, and so greater care has been taken to improve the fidelity of the simulations and to study their impact on heating estimates. To this end, the simulations are performed at very high horizontal and vertical resolutions to produce more physically consistent precipitation and heating structures, and the environmental forcing of the simulations is varied to produce a diversity of structures. Also, the simulated heating structures incorporated into the PR training algorithm are adjusted to account for differences between the model-simulated convective/stratiform precipitation proportions and the PR-estimated proportions. This adjustment ensures a near-balance of vertically integrated condensation and surface precipitation on a global basis. Further, the impact of precipitation depth biases due to the cloud-resolving simulations is mitigated by a echo top scaling of the training profiles.

In section 2, the satellite heating algorithm is described in detail. This section is followed by an evaluation of the errors of heating estimates relative to the PR training estimates in section 3, and an evaluation of errors due to the choice of cloud-resolving model simulations in section 4. In section 5, passive microwave estimates of latent and eddy sensible heating are combined with estimates of radiative heating and compared to rawinsonde-based analyses of total diabatic heating from two field campaigns. Finally, a summary and recommendations are offered in section 6.

2. Method

a. Overview

The latent heating algorithm has two components, which are illustrated schematically in Fig. 1. A training database is first created to establish the relationships between vertical latent heating profiles and upwelling microwave radiances, as they might be observed by a satellite passive microwave radiometer. This is accomplished by assigning vertical latent heating profiles to vertical precipitation profiles retrieved from spaceborne radar observations. Look-up tables derived from cloud-resolving model simulations are used to relate radar-derived precipitation profile features to vertical latent heating structures in the profile assignment procedure. The profile assignment procedure is similar to that of SH, but in addition, echo top information in stratiform precipitation regions is utilized.

To complete the training database, upwelling microwave radiances consistent with the radar-derived precipitation/latent heating profiles are either (a) calculated from the radar-retrieved 3D precipitation field or (b) assigned, if coincident satellite passive microwave observations are available. In the present study, microwave radiances are assigned, since the spaceborne radar data are derived from the PR, and coincident, upwelling microwave radiances from the TRMM Microwave Imager (TMI) are available within the 220 km-wide overlap swath. For algorithm applications to other satellite passive radiometers such as the Special Sensor Microwave/Imager, or the Advanced Microwave Scanning Radiometer-Earth Observing System, upwelling radiances would be calculated, since the channel frequencies and viewing geometry of these instruments differ from those of the TMI. In the present study, a general training database is created by assigning upwelling TMI radiances to coincident PR-estimated precipitation and latent

heating profiles, utilizing all coincident radiance/precipitation-heating profile pairs collected from one month of TRMM observations.

Once the training database is created, it may be applied to any TMI observations for which the training data are representative. Given a set of TMI radiance observations at a particular location, a Bayesian method is employed to composite precipitation or latent heating profiles in the training database and thereby construct profile estimates that are consistent with the TMI observations. The basic formulation of the Bayesian method is described in GO. In the following two subsections, the creation of the training database and radiometer latent heating algorithm are described in greater detail.

b. Generation of Training Data

The use of high-resolution, spaceborne radar derived precipitation profiles to train satellite microwave radiometer algorithms has been exploited in other remote sensing studies for improving estimates of precipitation (e.g., Bauer et al. 2001, Shin and Kummerow 2003, Kubota et al. 2007), but only in GO were these databases used to estimate latent heating. The primary difference between the latent heating algorithm of the current study and GO lies in the construction of the training database, described here.

As mentioned previously, GO utilized combined PR-TMI precipitation profile estimates as the foundation of their training database. The combined PR-TMI algorithm was described in Grecu et al. (2004), and it was demonstrated in that study that the combined PR-TMI estimates of precipitation were remarkably consistent with TRMM PR 2A-25 Version 5 algorithm estimates; see Iguchi et al. (2000) for a description of the PR 2A25 algorithm. However, in order to make clean intercomparisons of TMI-derived and

PR-derived precipitation/latent heating estimates in the present study, PR-only (2A-25 Version 6) estimates of precipitation profiles are used as the foundation of the training database. All 2A-25 profiles from July 2000, over ocean surfaces where precipitation was detected, are used to populate the training database. It was shown by GO that only small differences in subsequent satellite radiometer estimates of precipitation are incurred by selecting alternate monthly periods for training; i.e., one month of training data well represents the diversity atmospheric profiles that the satellite radiometer may encounter in any particular time period.

As described in the Introduction, a number of methods for assigning latent heating vertical profiles to precipitation vertical profiles from the PR have been developed. The basic principle behind several of these methods (Tao et al. 1990, 1993; Smith et al. 1994; Satoh and Noda 2001; Shige et al. 2004, 2007) is that under steady-state conditions, the net flux of precipitation out of (into) a given atmospheric layer must be compensated by a net source (sink) of precipitation particles within the layer. The net flux of precipitation is determined either from the precipitation fallout rate estimated using the PR algorithm, or from the estimated water content and a determination of the precipitation fallspeed and wind vertical velocity. The net rates of condensation/deposition (evaporation/ sublimation) provide the sources (sinks) of precipitation within the atmospheric layer, and these precipitation phase changes are related to latent heating through the specific latent heats of condensation or sublimation, i.e., L_v or L_s. Near the 0°C isotherm, either precipitation freezing or melting can occur, with the associated release or consumption of latent heat per unit mass given by L_f. Although the assumed steady-state conditions are not expected at the scales of the instantaneous footprint data to which the heating

algorithms are usually applied, it is understood that the steady state assumption may be appropriate for larger space or space-time averages of the satellite heating estimates. In Tao et al. (1993) and Shige et al. (2004, 2007) specifically, cloud-resolving model simulations are utilized to relate the unknown vertical structure of heating or cooling within an atmospheric layer to precipitation fluxes. And, instead of imposing a strict balance between layer-integrated heating and net vertical precipitation flux, only a scaling of the model heating profile by the precipitation flux is performed to allow for the effects of horizontal advection between convective and stratiform regions. These horizontal advection effects are represented, at least implicitly, by the cloud-resolving model simulations.

In the present study, the application of the steady-state precipitation principle follows the work of SH, but stratiform precipitation is treated in a different way. First, the PR precipitation profile observations are separated into convective and stratiform categories, since it is well-established that the cloud processes and vertical structures of latent heating in convective and stratiform regions are characteristically different; see Houze (1989). Typically, in convective regions over the tropical and subtropical oceans, latent heating profiles exhibit a positive maximum in the lower- to mid-troposphere due to condensation/deposition of water vapor in moist updrafts. In stratiform regions, heating profiles generally have a positive maximum in the upper-troposphere and a negative minimum due to evaporation of precipitation in the lower-troposphere. In addition to the convective and stratiform categories, PR precipitation profiles are separated by the echo top of the precipitation column, defined as the greatest altitude at which the PR-observed reflectivity exceeds the 17 dBZ minimum detection threshold. The second categorization

is important because the profile of heating is limited, approximately, by the top of the precipitation column.

Once a given PR precipitation profile is classified into a convective/stratiform and echo top category, a heating profile is assigned to it according to cloud-resolving model simulations of precipitation/latent heating profiles with the same characteristics. The apparent heat source (Yanai et al. 1973) is defined

$$Q_1 = \overline{\pi}\left(\frac{\partial\overline{\theta}}{\partial t} + \overline{\mathbf{V}}\bullet\nabla\overline{\theta} + \overline{w}\frac{\partial\overline{\theta}}{\partial z}\right), \tag{1}$$

where π is the exner function, defined

$$\pi = \left(p/1000\,hPa\right)^{R/c_p}. \tag{2}$$

Here, θ is potential temperature, $\mathbf{V}$ is the horizontal wind vector, w is the vertical wind velocity, p is pressure, R is the dry air constant, c_p is the specific heat of air at constant pressure, and the overbars represent large-scale horizontal averages. The right-hand-side of (1) therefore represents the large-scale average heating rate, and it is commonly evaluated using arrays of rawinsondes with spacings ~ 200 km; see Mapes et al. (2003). The apparent heat source can also be defined in terms of sources within the averaging area

$$\begin{aligned} Q_1 = {} & \frac{L_v}{c_p}\left(\overline{c}-\overline{e}\right) + \frac{L_f}{c_p}\left(\overline{f}-\overline{m}\right) + \frac{L_s}{c_p}\left(\overline{d}-\overline{s}\right) \\ & + \overline{\pi}\left(-\overline{V'\bullet\nabla\theta'} - \frac{1}{\overline{\rho}}\frac{\partial\overline{\rho}\,\overline{w'\theta'}}{dz}\right) + Q_R, \end{aligned} \tag{3}$$

where the first three terms on the right-hand-side are the average latent heating due to clouds and precipitation, the fourth and fifth terms are the horizontal and vertical

convergence of eddy sensible heat flux, the sixth term is the radiative heating rate (Q_R), and the primes indicate eddy perturbations with respect to the horizontal average.

In the present study, cloud-resolving model simulations are used to evaluate the latent and eddy sensible heat flux convergence terms of (3). Estimation of radiative heating would require information regarding cloud properties that are not obtainable from spaceborne radar or passive microwave observations alone, and therefore Q_R is not considered here. Strictly speaking, the eddy heating terms are functions of the averaging scale, and in the context of the current application the dimension of the model domain (~ 500 km) is proposed. In the deep-convective regimes of the tropics, the eddy sensible heat flux terms are relatively small compared to the latent heating terms.

Following SH, three long-term model simulations are performed to establish the relationships between PR-retrieved precipitation properties and the vertical latent+eddy heating profiles. The simulations are performed using a 2D version of the Goddard Cumulus Ensemble (GCE) model, described in Tao (2003) and Tao et al. (2003a). Simulations in 2D allow for relatively high horizontal resolution (250 m) runs on a large domain (512 km) for 30 days duration. It was shown by Lang et al. (2007) that better diurnal convective growth was achieved by decreasing the GCE model horizontal grid spacing from 1000 m, as in SH, to 250 m. It was also argued by Bryan et al. (2003) that simulations with resolutions ~100 m enable the physical processes of turbulence to occur, and these are essential for realistic representations of convective processes. In the vertical, a 41 level variable grid with higher resolution in the boundary layer (about 80 m) and lower resolution in the upper troposphere (about 1000 m) is utilized. The domain is periodic in the horizontal, which allows for long-term integrations of the model; see Tao

et al. (2003b). In addition to predictions of the basic thermodynamic variables and winds, the GCE bulk microphysics parameterization yields prognostic water contents for 5 hydrometeor classes, including nonprecipitating cloud liquid, rain, nonprecipitating cloud ice, snow, and graupel. Precipitation and latent+eddy heating profiles are evaluated every hour of simulation time at each model horizontal gridpoint.

The model is run for three 30-day periods, nudged by the large-scale advective forcing of temperature, humidity, and horizontal winds, using the method described in Tao et al. (2003b). Advective forcings are derived from rawinsonde array observations from the South China Sea Monsoon Experiment (SCSMEX) Northern Enhanced Sounding Array (NESA) over the period 00 UTC 18 May – 00 UTC 17 June 1998, the Tropical Ocean Global Atmosphere Coupled Ocean-Atmosphere Response Experiment (TOGA COARE) Intensive Flux Array (IFA) over the period 00 UTC 19 Dec. 1992 – 00 UTC 18 Jan. 1993, and the Kwajalein Experiment (KWAJEX) array over the period 06 UTC 6 Aug. – 06 UTC 5 Sept. 1999. The SCSMEX and TOGA COARE observations were analyzed by Johnson and Ciesielski (2002) and Lin and Johnson et al. (1996), respectively. The KWAJEX observations were subject to the constrained variational analysis described in Zhang et al. (2001). Although fairly diverse environmental forcing conditions are represented by the three field campaign observing periods, very general relationships between precipitation and latent+eddy heating cannot be established from this limited sample. However, for the purpose of testing the heating estimation method in applications to TRMM observations in the tropics and subtropics, these simulations are adequate. A more comprehensive strategy for sampling atmospheric environments is under development by the authors and will appear in a future study.

With the exception of the first 36 hours of each simulation, which represents the model spin-up period, at each hour of simulation time the instantaneous profiles of precipitation and latent+eddy heating are extracted from the simulation at each model horizontal gridpoint. The classification of each gridpoint as convective or stratiform is performed using the methodology described by Lang et al. (2003). The precipitation profiles at each gridpoint are used to evaluate the corresponding unattenuated radar reflectivities in 250 m thick bins along each profile; the reflectivities are then averaged in the horizontal to 4 km resolution to approximate the vertical and horizontal resolution of the PR (0.25 km and 4.3 km, respectively). The model simulated precipitation and latent+eddy heating profiles are also averaged in the horizontal to the same resolution. The averaged profiles are categorized as convective (stratiform) if the average convective (stratiform) model rain rate averaged over 4 km exceeds the average stratiform (convective) rain rate. The echo top of the precipitation column is determined by the altitude of the first average reflectivity bin, starting from the top of the model domain, that exceeds the 17 dBZ PR detection threshold. After the echo top of the precipitation column is determined, the profile is categorized by echo top in 2 km deep bins.

Once all of the simulated hydrometeor profiles are separated into convective/stratiform and echo top categories, all of the latent+eddy heating profiles in each category are averaged to produce lookup tables of the type shown in Fig. 2. These tables are similar to Fig. 6 of SH, but in their study, non-convective precipitation was separated into "stratiform" and "anvil" categories, where the category "anvil" represented all stratiform precipitation for which the precipitation top height was greater than the altitude of the melting level. Subsequently, "anvil" heating profiles were indexed by the

precipitation rate at the melting level. Since considerable variation of echo top heights occurs for both the "stratiform" and "anvil" categories, these categories were combined in the stratiform category of the present study. Note also that although qualitatively similar, the three model simulations produce different distributions of precipitation types. For example, the stratiform rain percentages are 34%, 41%, and 45% for the SCSMEX, TOGA COARE, and KWAJEX simulations, respectively. Generally, these percentages tend to be lower than the mean stratiform percentages estimated in the tropics and subtropics by the PR, which has an impact on the design of the algorithm; see the next subsection.

c. The PR Training Algorithm

Given an observed PR precipitation profile and its corresponding convective/stratiform classification, echo top, and precipitation profile, the cloud-model-based heating lookup tables are used to assign a latent+eddy heating profile as follows. If the profile is convective, then the observed echo top is used to identify the mean convective heating profile and surface rain rate from the convective heating table. If horizontal transports of precipitating hydrometeors could be neglected, then under steady state conditions the surface precipitation x L_v would equal the vertically-integrated heating in the profile. However, a significant percentage of condensate formed in the convective region is typically advected to stratiform areas, resulting in a surplus of heating relative to surface rain rate x L_v. Conversely, there is generally a deficit of heating in stratiform regions relative to rain rate x L_v due to the influx of condensate from the convective region. As an approximation, it is assumed here (as in SH) that the

convective and stratiform heating profiles are still proportional to surface rain rate. Therefore, if a PR observation is classified as convective, then

$$Q_1(z) - Q_R(z)\big|_{conv-PR} = \frac{\left\langle Q_1(z) - Q_R(z)\big|_{conv-model} \right\rangle}{\left\langle P_{conv-model} \right\rangle} \cdot P_{conv-PR} \qquad (4)$$

is an estimate of the convective heating profile corresponding to the PR-estimated convective rain rate, $P_{conv\text{-}PR}$, and $Q_1(z) - Q_R(z)|_{conv\text{-}model}$ is a convective latent+eddy heating profile and $P_{conv\text{-}model}$ is a convective rain rate, respectively, from the model simulations, and the brackets $\langle\ \rangle$ indicate an ensemble average over all convective model profiles in the appropriate echo top category of the lookup table. Similarly, if a PR observation is classified as stratiform,

$$Q_1(z) - Q_R(z)\big|_{strat-PR} = \frac{\left\langle Q_1(z) - Q_R(z)\big|_{strat-model} \right\rangle}{\left\langle P_{strat-model} \right\rangle} \cdot P_{strat-PR} \ . \qquad (5)$$

In estimating space- or space-time average heating profiles, the estimated average heating profile would be equal to an average of the PR footprint-scale estimates given by (4) and (5). However, since the advection of condensate from convective to stratiform regions in the model simulations may be different from the advection of condensate over a given area/period where (4) and (5) are applied, the estimated average, vertically-integrated heating and the estimated average surface rain rate x L_v over that area/period may not be equal. To make a correction for this effect, the model heating profiles in (4) and (5) are scaled by constant factors to yield

$$Q_1(z) - Q_R(z)\big|_{conv-PR-adj} = Q_1(z) - Q_R(z)\big|_{conv-PR} \cdot \beta \ , \qquad (6)$$

and

$$Q_1(z) - Q_R(z)\big|_{strat-PR-adj} = Q_1(z) - Q_R(z)\big|_{strat-PR} \cdot \gamma \ , \qquad (7)$$

where

$$\beta = \left(1 - f_{strat-model}\right)/\left(1 - f_{strat-PR}\right), \tag{8}$$

$$\gamma = f_{strat-model}/f_{strat-PR}, \tag{9}$$

and

$$f_{strat-model} = \overline{P_{strat-model}}/\overline{P_{total-model}}, \tag{10}$$

$$f_{strat-PR} = \overline{P_{strat-PR}}/\overline{P_{total-PR}}. \tag{11}$$

Here, the subscript "adj" refers to the adjusted convective and stratiform heating profiles, and "total" indicates combined convective and stratiform rain. The overbar indicates a space-time average, and in the present context, the model precipitation rates are averaged over all of the model volumes in a given 30-day simulation. The PR-estimated precipitation rates are averaged over all TRMM PR profiles over ocean during a one-month period. By adjusting the lookup table profiles using factors (8) and (9), the estimated total monthly vertically-integrated latent heating from PR is brought into close agreement with the total monthly surface rain rate x L_v.

Using the 30-day SCSMEX simulation and four months (April, July, October of 1998 and January of 1999) of PR data as a reference, mean values of β and γ equal to 1.42 and 0.64 respectively, are obtained. (Note: the specific choice of PR time period is not critical, since the β and γ values are similar for each month.) Similar algorithm applications based upon the TOGA COARE and KWAJEX simulations yield values of β equal to 1.26 and 1.17 and values of γ equal to 0.78 and 0.85, respectively. After the β and γ factors are applied, PR estimates of vertically-integrated latent heating and surface rain rate x L_v based upon the SCSMEX heating lookup table, averaged over all ocean regions and the four test months, are within 6%. If the heating estimation method had

been based upon a large spectrum of model simulations with different proportions of advected condensate, then the lookup table profiles might better represent global conditions, and β and γ could approach unity. However, the model could have its own inherent biases, and so some correction would likely be required. The use of a larger spectrum of model simulations is left for future studies.

d. Echo Top Correction

As noted by SH, the distribution of simulated radar echo tops from cloud resolving model simulations is different from the echo top distributions derived from PR observations. In the present study, the histograms of both convective and stratiform model-simulated echo tops is shifted toward higher echo tops relative to PR-observed echo top histograms. To help compensate for this shift, the indexed echo tops associated with each model-simulated heating profile are reduced by a factor of 0.9 in this study. This shift is justified because of a known bias in the cloud-resolving model ice microphysics, which leads to excessive graupel and snow production in GCE simulations; see Lang et al. (2007).

The model echo top scaling helps to bring the model-simulated echo top histograms from SCSMEX (NESA forcing; 18 May – 17 June 1998 period) and the PR-observed echo top histograms derived from observations over the same region and period of SCSMEX into better agreement. The correction is important because the depth of the PR estimated heating profiles is determined by the PR observed echo top. In the future, as the microphysical parameterizations of cloud-resolving models such as GCE improve, this echo top correction should no longer be necessary.

e. Radiometer Estimates of Latent Heating

Equations (6) and (7) are applied to all PR-retrieved precipitation profiles over ocean during a one-month period (July 2000) to create the foundation of the satellite radiometer algorithm training database. Since our study is currently limited to satellite radiometer heating estimates from TMI, the training database is completed by storing, in the database, the observed TMI radiances collocated with the PR-retrieved precipitation and heating profiles. In an attempt to match the resolution of the TMI observations, the PR precipitation/heating profiles in 3 x 3 neighborhoods centered on each TMI footprint are horizontally averaged and stored with the collocated TMI radiances. The collocation procedure establishes the relationships between TMI radiances and latent+eddy heating profiles. In order to examine the sensitivity of the TMI heating estimates to the cloud-resolving model simulations, separate training databases are created using the SCSMEX, TOGA COARE, and KWAJEX heating lookup tables.

Once created, the training databases are incorporated into the Bayesian estimation method of GO and applied to TMI radiance observations. Briefly, this algorithm does an initial search of the database to find vertical profiles that are consistent with climatological sea surface temperature conditions in the region of algorithm application, and it also finds those profiles that have echo tops close to a TMI radiance-based estimate of the echo top. The subset of database profiles with compatible sea surface temperatures and echo top characteristics is then examined to see how the observed TMI radiances and database radiances compare. (Note that in addition to the single-footprint radiances at all TMI channel frequencies and polarizations, the local variance of 85 GHz vertical

polarization radiances in a 3 x 3 footprint neighborhood is also used as a radiance predictor.) A Bayesian composite of the radiatively-consistent profiles in the database subset is created to yield the final TMI precipitation and heating profile estimates. A detailed description of the Bayesian algorithm may be found in GO.

3. Comparisons of Radiometer and Radar-Based Estimates

Here, estimates of Q_1-Q_R from the TMI algorithm are compared to estimates from the PR training algorithm. In this comparison, the TMI algorithm trained using the SCSMEX simulation latent heating lookup tables is utilized. The purpose of this test is to evaluate the consistency of TMI precipitation and heating estimates and the PR training data. Inconsistencies between the two sets of estimates would indicate a deficiency of relevant information on precipitation/heating in the TMI observations and/or a lack of relevant radiance predictors derived from the TMI observations.

Shown in Figs. 3a and 3b are the mean surface rain rates, stratiform rain fractions, and Q_1-Q_R at 7 km and 2 km altitudes for the period March 1998 – February 1999, based upon the TMI algorithm and the PR training algorithm, respectively. Note that although the TMI and PR mean rain rate distributions are similar, the distributions of stratiform rain fraction show some significant differences. In particular, the range of stratiform fractions from TMI is less than that of the PR, and the zonal gradient of PR stratiform fractions across the tropical Pacific Ocean is not evident in the TMI estimates. Regarding Q_1-Q_R, the distributions of upper-tropospheric heating from TMI and PR are quite similar. On the other hand, greater convective precipitation percentages from TMI, particularly in the eastern tropical Pacific, are associated with greater lower-tropospheric

heating from the TMI algorithm. The TMI convective bias also manifests itself in elevated lower-tropospheric heating in the South Pacific Convergence Zone and over the central Indian Ocean.

The regional variation of TMI Q_1-Q_R estimates and the differences with respect to the PR training algorithm are further illustrated in Fig. 4. To construct this figure, six test regions, defined in Table 1, are used to represent characteristically different latent heating regimes for which the heating vertical structure or its variability are generally different. Monthly-mean TMI and PR estimates of Q_1-Q_R profiles in each test region, computed for all 12 months during the March 1998 – February 1999 period, provide the basis for the statistics shown in Fig. 4. The bold, solid curves are the 12-month mean profiles, while the thin solid curves are the standard deviations of monthly values over the 12-month period. The dashed and dash-dot curves represent the biases and error standard deviations, respectively, of the TMI Q_1-Q_R monthly estimates relative to the PR monthly estimates.

First, note from Fig. 4 that the TMI algorithm appears to capture regional variations of latent heating vertical structure. So, for example, the estimated shallow convective heating associated with trade wind cumulus and precipitating congestus over the north central Pacific (NCPAC) is in marked contrast to the deep heating structures of the inter-tropical convergence zone regimes, which are dominated by organized convective systems. The variation of estimated heating profiles tends to be greatest in the upper troposphere, at least in the deep convective regimes near the equator. The bias of TMI estimates relative to the PR in the upper troposphere is generally small; however, in the lower troposphere, the TMI estimates show a positive bias of varying magnitude. As

noted previously, this positive bias is most pronounced in the eastern Pacific, with a maximum magnitude of 1.9 K day^{-1}, and therefore it has a significant impact on the vertical heating distribution. TMI error standard deviations relative to PR are also greatest in the lower troposphere, and the magnitudes of these errors are of the same order as the month-to-month variation of heating.

The vertical distributions of biases and error standard deviations suggest that it is difficult for the current TMI algorithm to accurately quantify Q_1-Q_R in the lower troposphere, or at least it is difficult for the algorithm to reproduce the lower-tropospheric heating variations derived from the PR observations. An examination of instantaneous, footprint-scale estimates of heating from the TMI and PR indicate a lack of sensitivity of the TMI predictors (both radiances and 85 GHz radiance variances) to variations of convective/stratiform proportion, particularly in regimes such as the eastern tropical Pacific. In the eastern tropical Pacific, specifically, Shige et al. (2008) present evidence that precipitation systems have a tendency to be shallower, with weaker updrafts and less production of ice-phase precipitation. For precipitation systems of this type, the heating algorithm's convective/stratiform separation must rely on lower-frequency microwave emission signatures, which are less descriptive of convective/stratiform conditions in weakly-organized systems; see Hong et al. (1999). A partial correction of the lower-tropospheric bias using a maximum radiance difference predictor is examined in the Summary and Recommendations section; however, a full correction will likely require the construction of more specific algorithm training databases that target regional climatic conditions.

4. Sensitivity to the Cloud Resolving Model Tables

Here, the objective is to determine how the specific choice of training data affect regional estimates of heating at monthly scale. The selected regions are the six regions previously described in Section 3; see Table 1. As in the last section, the heating algorithm trained using the SCSMEX simulation is first applied to TMI data from each of the 12 months from March 1998 through February 1999. Monthly, regional-mean Q_1-Q_R is calculated for each of the six regions in the table. Next, the TMI algorithm trained using the TOGA COARE and KWAJEX simulations is alternately applied to the 12 months of regional data, and monthly, regional-mean Q_1-Q_R is calculated using these two variations of the algorithm. For each month and region, a reference Q_1-Q_R is then computed as the arithmetic mean of the SCSMEX, TOGA COARE, and KWAJEX estimates, following the work of Smith et al. (2006). The biases and error standard deviations of the SCSMEX monthly, regional-mean estimates are then evaluated relative to the reference mean estimates. Since the reference estimates are based on only 3 different lookup tables, the computed biases and error standard deviations are only intended to provide a rough measure of the magnitudes of potential errors that might be incurred by using only a single lookup table to train the TMI algorithm.

Shown in Fig. 5 are the 12-month mean and standard deviation profiles of the monthly, regional-mean SCSMEX estimates, as well as the bias and error standard deviation profiles of the SCSMEX-based estimates relative to the reference estimates. In the mean, the SCSMEX-based estimates deviate from the reference by at most 0.6 ^{o}K day^{-1} at an altitude near 6 km. Error standard deviations of the SCSMEX-based estimates, on the order of 0.5 ^{o}K day^{-1} or less, are relatively small. It might be concluded that as

long as the simulations utilized to generate a given lookup table are representative of the region where the algorithm is applied, then the heating estimates will not be too sensitive to the details of the table. However, in light of the regionally-dependent heating biases noted in section 3, regionally-dependent or regime-dependent training of the TMI algorithm should help to reduce heating biases, and lookup tables consistent with the regions or regimes selected for training should be developed.

5. Evaluation of Radiometer Estimates vs. Field Observations

In this section, satellite estimates of surface rain rate, Q_1-Q_R, and Q_1 are compared to rawinsonde-based estimates of surface rain rate and Q_1. The satellite estimates of surface rain rate and Q_1-Q_R are derived from the TMI algorithm trained using the SCSMEX cloud model lookup tables, as described previously. Satellite estimates of Q_1 are derived by combining the TMI Q_1-Q_R with estimates of Q_R from the Hydrologic cycle and Earth's Radiation Budget (HERB) algorithm originally described in L'Ecuyer and Stephens (2003, 2007). Briefly, HERB synthesizes ice cloud microphysical property information from VIRS, liquid cloud properties, precipitation profiles, SST, and water vapor retrievals from the TRMM TMI, and vertical profiles of temperature and humidity from European Center for Medium-range Weather Forecasts (ECMWF) reanalyses, to characterize the three-dimensional structure of clouds and precipitation in the atmosphere. These provide input to a broadband radiative transfer model that simulates vertical profiles of upwelling and downwelling longwave and shortwave radiative fluxes and their convergence/divergence, defining the vertical profile of atmospheric Q_R. A

comprehensive description of the latest version of the HERB algorithm and its uncertainty characteristics can be found in L'Ecuyer and McGarragh (2009).

Independent estimates of surface rain rate and Q_1 are derived from enhanced sounding network and surface data that were collected during field campaign intensive observing periods. Data collected from the Northern Enhanced Sounding Array (NESA) during the intensive observing period of SCSMEX (5 May – 20 June 1998) were analyzed by Johnson and Ciesielski (2002). The sounding array data were augmented with large-scale analyses of pressure, temperature, humidity, and winds to estimate the mean vertical profiles of Q_1 and Q_2 over the NESA. By vertically integrating Q_2 to obtain the net atmospheric sink of humidity, and adding to this estimates of surface evaporation from a combination of ship measurements and analyzed fluxes, Johnson and Ciesielski (2002) also estimated surface rain rate as a residual of the moisture budget. For the purpose of the intercomparisons in the present study, a subset of the intensive observing period (15 May – 20 June 1998) was selected, due to the increased potential for biases in the analyzed winds during the monsoon pre-onset period (prior to 15 May, approximately); see Johnson and Ciesielski (2002).

More recently, estimates of Q_1 and Q_2 were derived from rawinsonde network data collected during the Mirai Indian Ocean cruise for the Study of the Madden-Julian-Oscillation convection Onset (MISMO; Oct. – Dec. 2006). Surface rain rates were estimated as a residual of the moisture budget in a manner similar to Johnson and Ciesielski (2002), using additional shipboard flux measurements. MISMO estimates of surface rain rate and Q_1 were provided by Dr. Masaki Katsumata of the Japanese Agency for Marine-Earth Science and Technology (JAMSTEC). During the period 31 October –

26 November 2006, the MISMO rawinsonde network was fully operational, and so data from that period were selected for the purpose of intercomparisons in the present study. A description of the synoptic-scale processes over the MISMO network during this period is given in Katsumata et al. (2009b).

Time series of surface rain rate, TMI Q_1-Q_R, combined TMI/VIRS Q_1, and rawinsonde Q_1 over the SCSMEX NESA are presented in Fig. 6a. A 3-day running mean filter is applied to all time series to reduce the effects of random sampling errors; see Mapes et al. (2003) for a discussion of the impact of temporal averaging on the errors of rawinsonde-based heating estimates. Note that there is a fairly good correspondence between TMI and rawinsonde-derived estimates of surface rain rate, in spite of the very different methods employed to make these estimates. Nevertheless, there are some significant differences between the time series prior to 15 May, near 25 May, and after 7 June, 1998. By subsampling the rawinsonde time series within 1.5 hours of the TMI overpass times (not shown), it was determined that the differences prior to 15 May and near 25 May are likely due to insufficient temporal sampling by the TMI (~1.4 day^{-1}) relative to that of the rawinsonde array (2-4 day^{-1}). The differences after 7 June are not affected greatly by sampling, and the lighter precipitation during that period may be difficult for TMI to detect. In spite of the sampling differences, the mean rain rates from the TMI (10.3 mm day^{-1}) and the rawinsonde analyses (9.4 mm day^{-1}) over the entire period are close in magnitude.

When the TMI/VIRS estimates of Q_R are added to the TMI estimates of Q_1-Q_R, the resulting heating estimate is a close approximation to Q_1. Only eddy sensible heat flux contributions outside regions of precipitation are not included in the TMI/VIRS Q_1

estimate, and these eddy contributions primarily impact the heating of the boundary layer; see Newell et al. (1969); Schaack et al. (1990). Aside from the periods of undersampling by TMI, the Q_1 time series from TMI/VIRS and the rawinsonde analyses are qualitatively similar. The main notable differences are the peak magnitudes of heating, which are higher in the TMI/VIRS series. The mean heating profiles for the entire period, normalized by the mean surface rain rates, are shown in Fig. 6b. The higher peak magnitude of Q_1 from the TMI/VIRS is evident from the figure, and the impact of radiative cooling is nearly uniform in the vertical. Although the vertical gradient of TMI/VIRS heating with altitude is similar to that of the rawinsonde analyses below the level of peak heating (about 7.5 km), there is a sharper falloff of TMI/VIRS heating with altitude above that level. The TMI estimates of rainfall show a deficiency of rain relative to the rawinsonde Q_2 budget analyses after June 11, which might account for the deficiency of Q_1 above 7.5 km; however, radiative cooling is particularly strong near 10 km altitude, and so the ingredients of both the Q_1-Q_R and Q_R satellite estimates should be examined for potential biases. This work is left for a future study. Nevertheless, the addition of TMI/VIRS radiative cooling profiles to the TMI Q_1-Q_R profiles yields estimates of Q_1 that are a much better approximation to the rawinsonde estimates of Q_1 than if they were omitted.

TMI sampling of the MISMO array (1.2 day^{-1}) is less than that of the NESA array, and the correspondence between the TMI and rawinsonde estimates of surface rain rate is weaker; see Fig. 7a. Subsampling of the MISMO rawinsonde time series near the TMI overpass times (not shown) does not necessarily result in a better correspondence with the TMI time series. The bias of the TMI Q_1 estimates in the time series of Fig. 7a

clearly follows the bias of the TMI rain estimates. The total bias of the TMI rain rates (12.4 mm day^{-1}) relative to the rawinsonde rain estimates (9.5 mm day^{-1}) over the entire observation period is significant. After normalization by rain rate, the mean TMI/VIRS and rawinsonde Q_1 heating profiles are similar; see Fig. 7b. The TMI/VIRS mean Q_1 profile exhibits a slightly stronger peak heating near 7.5 km, and weaker heating at higher and lower altitudes, relative to the rawinsonde mean Q_1 profile.

6. Summary and Recommendations

In this study, satellite passive microwave sensor observations from the TMI are utilized to make estimates of latent+eddy sensible heating rates (Q_1-Q_R). The TMI heating algorithm, TRAIN, is calibrated using relatively accurate PR-based estimates of heating, which are collocated with the TMI observations over a one month period to create a training dataset. The TMI heating estimation technique is based upon a Bayesian methodology originally described in GO, but with noted improvements.

Estimates of Q_1-Q_R from TMI compare favorably with the PR training estimates and show only modest sensitivity to the cloud-resolving model simulations of heating used to construct the training data. Moreover, the net condensation in the corresponding annual mean satellite latent heating profile is within a few percent of the annual mean surface precipitation rate over the tropical and subtropical oceans where the algorithm is applied. Comparisons of Q_1 produced by combining TMI Q_1-Q_R with estimates of Q_R from L'Ecuyer and McGarragh (2009) show reasonable agreement with rawinsonde-based analyses of Q_1 from two field campaigns, although the satellite estimates exhibit heating

profile structure with sharper and more intense heating peaks than the rawinsonde estimates.

Although the emphasis in this study has been on the characterization of errors in microwave radiometer heating estimates, more work is required to (a) reduce biases in regional heating estimates, particularly in the eastern Pacific where estimated lower-tropospheric heating is significantly greater than the PR training estimates, and (b) produce a useful model of the random errors in heating estimates that covers the range of space-time scales considered in weather and climate applications. Regarding (a), regional or climate-regime dependent training of the heating method may be required, since the current method is only designed to minimize the heating bias on a global basis. Such regional training has been applied to microwave precipitation estimation by Shin and Kummerow (2003) with some success. With respect to (b), an error model for TMI precipitation estimates was developed by Olson et al. (2006) to span scales from instantaneous microwave footprints to seasonal averages at 2.5° resolution. The form of such an error model should also be applicable to estimates of Q_1-Q_R, but first, the space-time correlation of random heating errors must be estimated to in order to produce a credible model.

Another strategy to reduce heating bias and random error is to introduce additional radiance predictors into the estimation method. In the current method, only the radiances at each TMI channel frequency and the local variance of 85 GHz vertical polarization radiances in a 3 x 3 footprint neighborhood are utilized to estimate heating. In a preliminary test, these radiance predictors are augmented by the 19 GHz horizontal polarization "maximum difference" as an additional predictor. The radiance maximum

difference is defined here as the maximum difference between the radiance of a given central footprint and the radiances of all neighboring footprints in a small grid surrounding the central footprint; e.g., see Hong et al. (1999). In the present implementation, the grid of footprints includes all footprints within one scan line and three scan positions of the central footprint, forming a an approximately square region 28 km on a side. The 19 GHz maximum difference radiance predictor identifies local maxima of microwave rain emission that may be associated with convective precipitation. What prompted the choice of this additional predictor is the misidentification by the current TMI algorithm of shallow, uniform rain fields as partially convective, and this leads to greater estimated convective heating than that determined from the PR. When the additional predictor is included in the estimation method and applied to TMI data from the March 1998 – February 1999 period, the stratiform precipitation fraction in the TEPAC region increases only 2%, but the high bias in lower-tropospheric heating is reduced by 18% at 3 km altitude and 28% at 4 km altitude. The TEPAC mean Q_1-Q_R profiles with and without the new radiance predictor are shown in Fig. 8. Tests such as this one illustrate the potential benefits of exploiting new radiance information in radiometer-based heating estimation methods.

It should be emphasized that the microwave radiometer estimates of Q_1-Q_R in this study include eddy sensible heat flux contributions, but only where the algorithm is applied; i.e., in regions of significant precipitation. Outside regions of precipitation, the contributions of sensible heat fluxes to atmospheric heating, particularly in the boundary layer, are significant. Therefore, for global energy budget applications, an effort to estimate boundary layer heating using satellite observations, in conjunction with model-

based analyses, should be undertaken. The estimation of heating profiles over land, although much more difficult from passive microwave radiometry due to the reduced precipitation signal, must also be considered if the atmospheric energy budget is to be "closed". Since land regions tend to be data-rich relative to ocean regions, large-scale analyses of pressure, temperature, humidity, and winds could be adjusted using satellite passive microwave and visible/infrared estimates of water and energy fluxes to provide improved estimates of diabatic heating; see Xie et al. (2004). The estimation of boundary layer heating and the extension of the heating estimation method to land regions will be the subjects of future studies by the authors.

Acknowledgments The authors greatly appreciate the efforts of Richard Johnson and Paul Ciesielski of Colorado State University and Masaki Katsumata of JAMSTEC, who made available estimates of surface rain rate and heating profiles from the SCSMEX and MISMO campaigns, respectively, and provided valuable discussions of the quality of their estimates. The advective forcing for the KWAJEX cloud-resolving simulation was kindly provided by Minghua Zhang of Stony Brook University. We also thank Shoichi Shige of Osaka Prefecture University and Stephen Lang of Science Systems and Applications, Inc., for their insights regarding the modeling of convection and heating algorithm development. This research was supported by NASA's Energy and Water cycle Study (NEWS) and Precipitation Measurement Missions (PMM) programs.

References

Bauer, P., P. Amayenc, C. D. Kummerow, and E. A. Smith, 2001: Over-ocean rainfall retrieval from multisensor data of the Tropical Rainfall Measuring Mission. Part II: Algorithm implementation. *J. Atmos. Oceanic Tech.*, **18**, 1838-1855.

Bryan, G. H., J. C. Wyngaard, and J. M. Fritsch, 2003: Resolution requirements for the simulation of deep moist convection. *Mon. Wea. Rev.*, **131**, 2394-2416.

Grecu, M., W. S. Olson, and E. N. Anagnostou, 2004: Retrieval of precipitation profiles from multiresolution, multifrequency, active and passive microwave observations. *J. Appl. Meteor.*, **43**, 562-575.

Grecu, M., and W. S. Olson, 2006: Bayesian estimation of precipitation from satellite passive microwave observations using combined radar-radiometer retrievals. *J. Appl. Meteor. and Climatol.*, **45**, 416-433.

Hartmann, D.L., H. H. Hendon, and R. A. Houze, 1984: Some implications of the mesoscale circulations in tropical cloud clusters for large-scale dynamics and climate. *J. Atmos. Sci.*, **41**, 113-121.

Hong, Y., C. D. Kummerow, and W. S. Olson, 1999: Separation of convective and stratiform precipitation using microwave brightness temperatures. *J. Appl. Meteor.*, **38**, 1195-1213.

Houze, R. A., Jr., 1989: Observed structure of mesoscale convective systems and implications for large-scale heating. *Quart. J. Roy. Meteor. Soc.*, **115**, 425-461.

Iguchi, T., T. Kozu, R. Meneghini, J. Awaka, and K. Okamoto, 2000: Rain-profiling algorithm for the TRMM Precipitation Radar. *J. Appl. Meteor.*, **39**, 2038-2052.

Johnson, R. H., and P. E. Ciesielski, 2002: Characteristics of the 1998 summer monsoon onset over the northern South China Sea. *J. Meteor. Soc. Japan*, **80**, 561-578.

Katsumata, M., S. Mori, T. Ushiyama, Y.-M. Kodama, and S. Satoh, 2009a: An improved version of the PRH latent heating estimation algorithm based on the observed vertical structure of precipitating systems. *J. Climate*, submitted.

Katsumata, M., R. H. Johnson, and P. E. Ciesielski, 2009b: Observed synoptic-scale processes associated with the MJO onset of the Indian Ocean during MISMO. *J. Atmos. Sci.*, submitted.

Kubota, T., S. Shige, H. Hashizume, K. Aonashi, N. Takahashi, S. Seto, M. Hirose, Y. N. Takayabu, T. Ushio, K. Nakagawa, K. Iwanami, M. Kachi, and K. Okamoto, 2007:

Global precipitation map using satellite-borne microwave radiometers by the GSMaP project: Production and validation. *IEEE Trans. Geosci. Rem. Sensing*, **45**, 2259 – 2275.

Lang, S., W.-K. Tao, J. Simpson, and B. Ferrier, 2003: Modeling of convective–stratiform precipitation processes: Sensitivity to partitioning methods. *J. Appl. Meteor.*, **42**, 505-527.

Lang, S., W.-K. Tao, R. Cifelli, W. Olson, J. Halverson, S. Rutledge, and J. Simpson, 2007: Improving simulations of convective systems from TRMM LBA: Easterly and westerly regimes. *J. Atmos. Sci.*, **64**, 1141-1164.

Lau, K.-M., and L. Peng, 1987: Origin of low-frequency (intraseasonal) oscillations in the tropical atmosphere. Part I: Basic theory. *J. Atmos. Sci.*, **44**, 950-972.

L'Ecuyer, T. S., and G. L. Stephens, 2003: The tropical oceanic energy budget from the TRMM perspective. Part I: Algorithm and uncertainties. *J. Climate*, **16**, 1967-1985.

L'Ecuyer, T. S. and G. L. Stephens, 2007: The tropical atmospheric energy budget from the TRMM perspective. Part II: Evaluating GCM representations of the sensitivity of regional energy and water cycles to the 1998-99 ENSO cycle. *J. Climate,* **20**, 4548-4571.

L'Ecuyer, T. S. and G. McGarragh, 2009: A ten year climatology of atmospheric radiative heating and its vertical structure from TRMM observations. *J. Climate*, submitted.

Lin, X., and R. H. Johnson, 1996: Heating, moistening and rainfall over the western Pacific warm pool during TOGA COARE. *J. Atmos. Sci.*, **53**, 3367-3383.

Mapes, B. E., and R. A. Houze, Jr., 1995: Diabatic divergence profiles in western Pacific mesoscale convective systems. *J. Atmos. Sci.*, **52**, 1807-1828.

Mapes, B. E., P. E. Ciesielski, and R. H. Johnson, 2003: Sampling errors in rawinsonde-array budgets. *J. Atmos. Sci.*, **60**, 2697-2714.

Newell, R. E., D. G. Vincent, T. G. Dopplick, D. Ferruzza, and J. W. Kidson, 1969: The energy balance of the global atmosphere. *The Global Circulation of the Atmosphere*, G. A. Corby, Ed., Royal Meteorological Society, London, 42-90.

Nitta, T., 1970: A study of the generation and conversion of eddy available potential energy in the Tropics. *J. Meteor. Soc. Japan*, **48**, 524-528.

Nitta, T., 1972: Energy budget of wave disturbances over the Marshall Islands during the years of 1956 and 1958. *J. Meteor. Soc. Japan*, **50**, 71-84.

Puri, K., 1987: Some experiments on the use of tropical diabatic heating information in initial state specification. *Mon. Wea. Rev.*, **115**, 1394-1406.

Satoh, S., and A. Noda, 2001: Retrieval of latent heating profiles from TRMM radar data. Preprints, *30th International Conf. on Radar Meteorology*, Munich, Germany, 340-342.

Schaack, T. K., D. R. Johnson, and M.-Y. Wei, 1990: The three-dimensional distribution of atmospheric heating during the GWE, *Tellus*, **42A**, 305-327.

Schumacher, C., R. A. Houze Jr., and I. Kraucunas, 2004: The tropical dynamical response to latent heating estimates derived from the TRMM Precipitation Radar. *J. Atmos. Sci.*, **61**, 1341-1358.

Shige, S., Y. N. Takayabu, W. K. Tao, and D. E. Johnson, 2004: Spectral retrieval of latent heating profiles from TRMM PR data. Part I: Development of a model-based algorithm. *J. Appl. Meteor.*, **43**, 1095-1113.

Shige, S., Y. N. Takayabu, W.-K. Tao, and C.-L. Shie, 2007: Spectral retrieval of latent heating profiles from TRMM PR data. Part II: Algorithm improvement and heating estimates over tropical ocean regions. *J. Appl. Meteor. Climatol.*, **46**, 1098-1124.

Shige, S., T. Watanabe, H. Sasaki, T. Kubota, S. Kida, and K. Okamoto 2008: Validation

of western and eastern Pacific rainfall estimates from the TRMM PR using a radiative transfer model. *J. Geophys. Res. Atmos.*, **113**, D15116.

Shin, D.-B. and C. Kummerow, 2003: Parametric rainfall retrieval algorithms for passive microwave radiometers. *J. Appl. Meteor.*, **42**, 1480-1496.

Smith, E. A., X. Xiang, A. Mugnai, and G. J. Tripoli, 1994: Design of an inversion-based precipitation profile retrieval algorithm using an explicit cloud model for initial guess microphysics. *Meteorol. Atmos. Phys.*, **54**, 53-78.

Smith, T. M., P. A. Arkin, J. J. Bates, G. J. Huffman, 2006: Estimating bias of satellite-based precipitation estimates. *J. Hydrometeor.*, **7**, 841-856.

Tao, W.-K., J. Simpson, S. Lang, M. McCumber, R. Adler, and R. Penc, 1990: An algorithm to estimate the heating budget from vertical hydrometeor profiles. *J. Appl. Meteor.*, **29**, 1232-1244.

Tao, W.-K., S. Lang, J. Simpson, and R. Adler, 1993: Retrieval algorithms for estimating the vertical profiles of latent heat release. *J. Met. Soc. Japan*, **71**, 685-700.

Tao, W.-K., 2003: Goddard Cumulus Ensemble (GCE) Model: Application for understanding precipitation processes. *AMS Meteorological Monographs*: *Cloud*

Systems, Hurricanes, and the Tropical Rainfall Measuring Mission (TRMM) -- A Tribute to Dr. Joanne Simpson, **29**, 107-138.

Tao, W.-K., J. Simpson, D. Baker, S. Braun, M.D. Chou, B. Ferrier, D. Johnson, A. Khain, S. Lang, B. Lynn, C.-L Shie, D. Starr, Y. Wang, and P. Wetzel, 2003a: Microphysics, radiation and surface processes in the Goddard Cumulus Ensemble (GCE) model. *Meteorol. Atmos. Phys.*, **82**, 97-137.

Tao, W.-K., C.-L. Shie, J. Simpson, S. Braun, R. H. Johnson, and P. E. Ciesielski, 2003b: Convective systems over the South China Sea: Cloud-resolving model simulations. *J. Atmos. Sci.*, **60**, 2929-2956.

Valdes, P. J., and B. J. Hoskins, 1989: Linear stationary wave simulations of the time-mean climatological flow. *J. Atmos. Sci.*, **46**, 2509-2527.

Xie, S., R. T. Cederwall, and M. Zhang, 2004: Developing long-term single-column model/cloud system-resolving model forcing data using numerical weather prediction products constrained by surface and top of the atmosphere observations. *J. Geophys. Res. Atmos.*, **109**, D01104.

Yanai, M., S. Esbensen, and J.-H. Chu, 1973: Determination of bulk properties of tropical cloud clusters from large-scale heat and moisture budgets. *J. Atmos. Sci.*, **30**, 611-627.

Yanai, M., B. Chen, and W.-W. Tung, 2000: The Madden-Julian Oscillation observed during the TOGA COARE IOP: Global view. *J. Atmos. Sci.*, **57**, 2374-2396.

Zhang, M. H., J. L. Lin, R. T. Cederwall, J. J. Yio, and S. C. Xie, 2001: Objective analysis of ARM IOP data: Method and sensitivity. *Mon. Wea. Rev.*, **129**, 295-311.

Tables

Table 1. Regions used in the error analysis of TMI Q_1-Q_R estimates.

Region	Latitude Range	Longitude Range
Northwest Pacific Ocean (NWPAC)	20° N – 30° N	130° E – 160° E
North Central Pacific Ocean (NCPAC)	15° N – 25° N	180° W – 150° W
Tropical Western Pacific Ocean (TWPAC)	0° – 10° N	130° E – 160° E
Tropical Eastern Pacific Ocean (TEPAC)	0° – 10° N	130° W – 100° W
Tropical Central Indian Ocean (TCIO)	10° S – 0°	60° E – 90° E
Tropical Central Atlantic Ocean (TCATL)	0° – 10° N	45° W – 15° W

Figure Captions

Fig. 1. Flow diagram for the PR training algorithm and TMI latent heating algorithm.

Fig. 2. Latent+eddy heating profile lookup tables derived from SCSMEX simulations (top row) and TOGA COARE simulations (bottom row). Colors indicate the magnitudes of the mean heating rates, divided by the mean surface rain rates, of model profiles binned by echo top, plotted on the abscissa. Convective and stratiform heating tables are shown in the left and right columns, respectively.

Fig. 3. Mean estimates of surface rainfall rate, stratiform rain proportion, and Q_1-Q_R at 7 km and 2 km altitudes from (a) the TMI algorithm, and (b) the PR training algorithm, for the period 1 March 1998 – 28 February 1999. Estimates from the TMI have been subsetted to include only those coinciding with the PR swath.

Fig. 4. Profiles of the mean, standard deviation, bias, and error standard deviation of TMI monthly-mean estimates of Q_1-Q_R for the six regions defined in Table 1, over the period 1 March 1998 – 28 February 1999. Biases and error standard deviations are based upon the differences of estimates from the TMI algorithm and the PR training algorithm. Estimates from the TMI have been subsetted to include only those coinciding with the PR swath.

Fig. 5. Same as Fig. 4, but the biases and error standard deviations are estimated potential errors due to the choice of heating lookup table. The biases and error standard

deviations are based upon the differences between the TMI algorithm (using the SCSMEX heating lookup table) and an average of TMI algorithm estimates derived using the SCSMEX, TOGA COARE, and KWAJEX heating lookup tables.

Fig. 6a. Time series of surface rain rates from the TMI algorithm and the rawinsonde moisture budget (top panel), TMI estimates of Q_1-Q_R (second from top), TMI/VIRS combined estimates of Q_1 (third from top), and rawinsonde analyses of Q_1 (bottom panel) for the period 15 May – 20 June, 1998, over the SCSMEX NESA.

Fig. 6b. Rain rate normalized mean profiles of TMI-estimated Q_1-Q_R, TMI/VIRS combined estimates of Q_1, and rawinsonde analysis estimates of Q_1 for the period 15 May – 20 June, 1998, over the SCSMEX NESA.

Fig. 7a. Same as Fig. 6a, but for the period 31 October – 26 November, 2006, over the MISMO sounding array.

Fig. 7b. Same as Fig. 6b, but for the period 31 October – 26 November, 2006, over the MISMO sounding array.

Fig. 8. Estimates of the mean profiles of Q_1-Q_R over the TEPAC region (see Table 1) for the period 1 March 1998 – 28 February 1999, based upon the TMI algorithm and an alternative TMI algorithm (Alt) that utilizes an additional radiance predictor for the local intensity of microwave emission in the 19 GHz horizontal polarization channel.

Fig. 1. Flow diagram for the PR training algorithm and TMI latent heating algorithm.

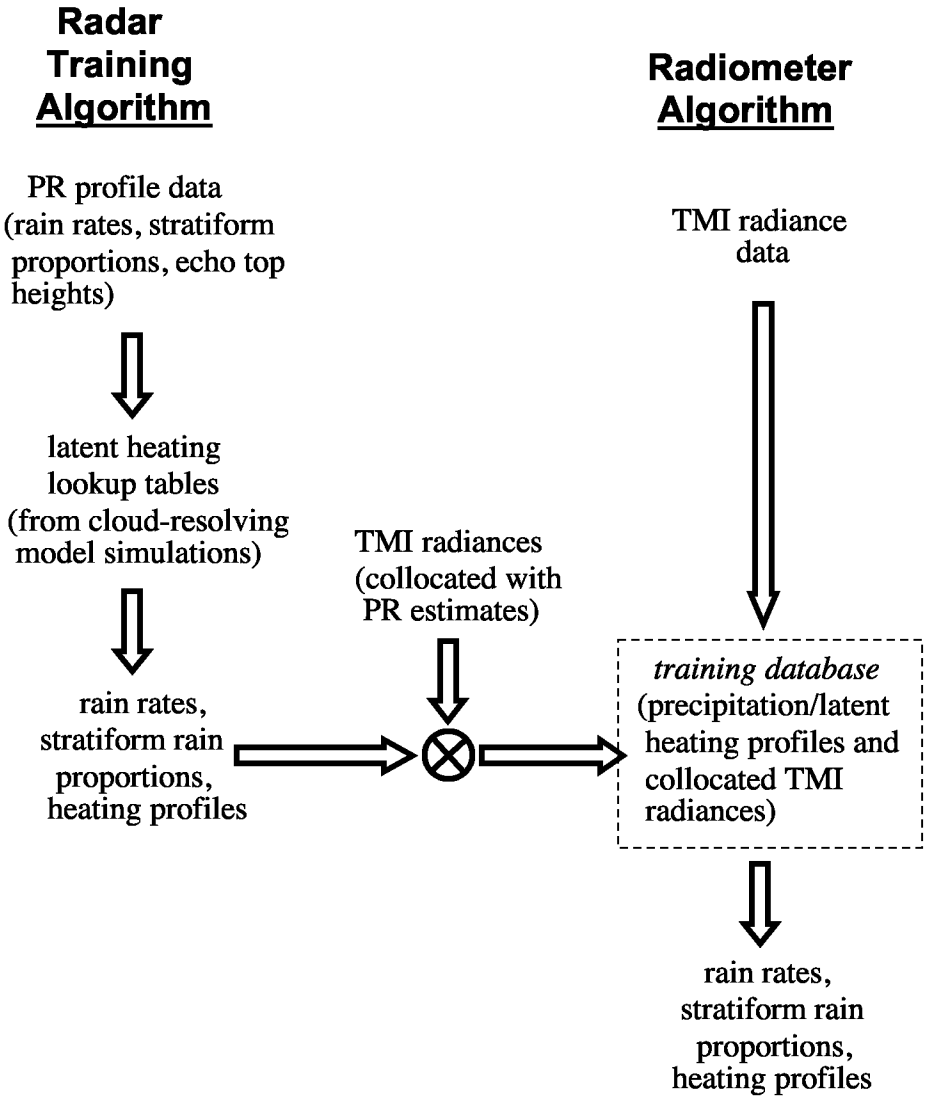

Fig. 2. Latent+eddy heating profile lookup tables derived from SCSMEX simulations (top row) and TOGA COARE simulations (bottom row). Colors indicate the magnitudes of the mean heating rates, divided by the mean surface rain rates, of model profiles binned by echo top, plotted on the abscissa. Convective and stratiform heating tables are shown in the left and right columns, respectively.

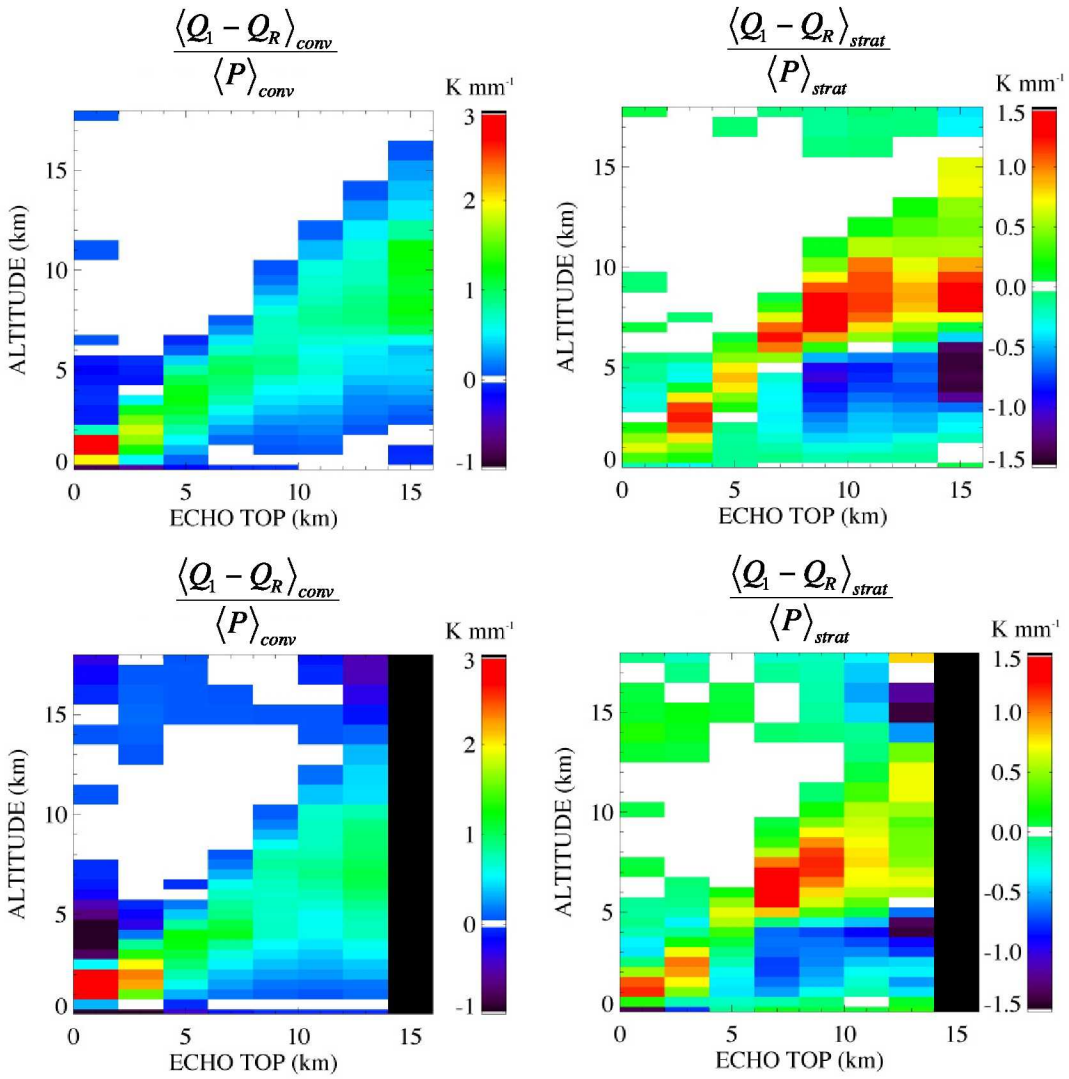

Fig. 3. Mean estimates of surface rainfall rate, stratiform rain proportion, and Q_1-Q_R at 7 km and 2 km altitudes from (a) the TMI algorithm, and (b) the PR training algorithm, for the period 1 March 1998 – 28 February 1999. Estimates from the TMI have been subsetted to include only those coinciding with the PR swath. **Fig. 3(a)**

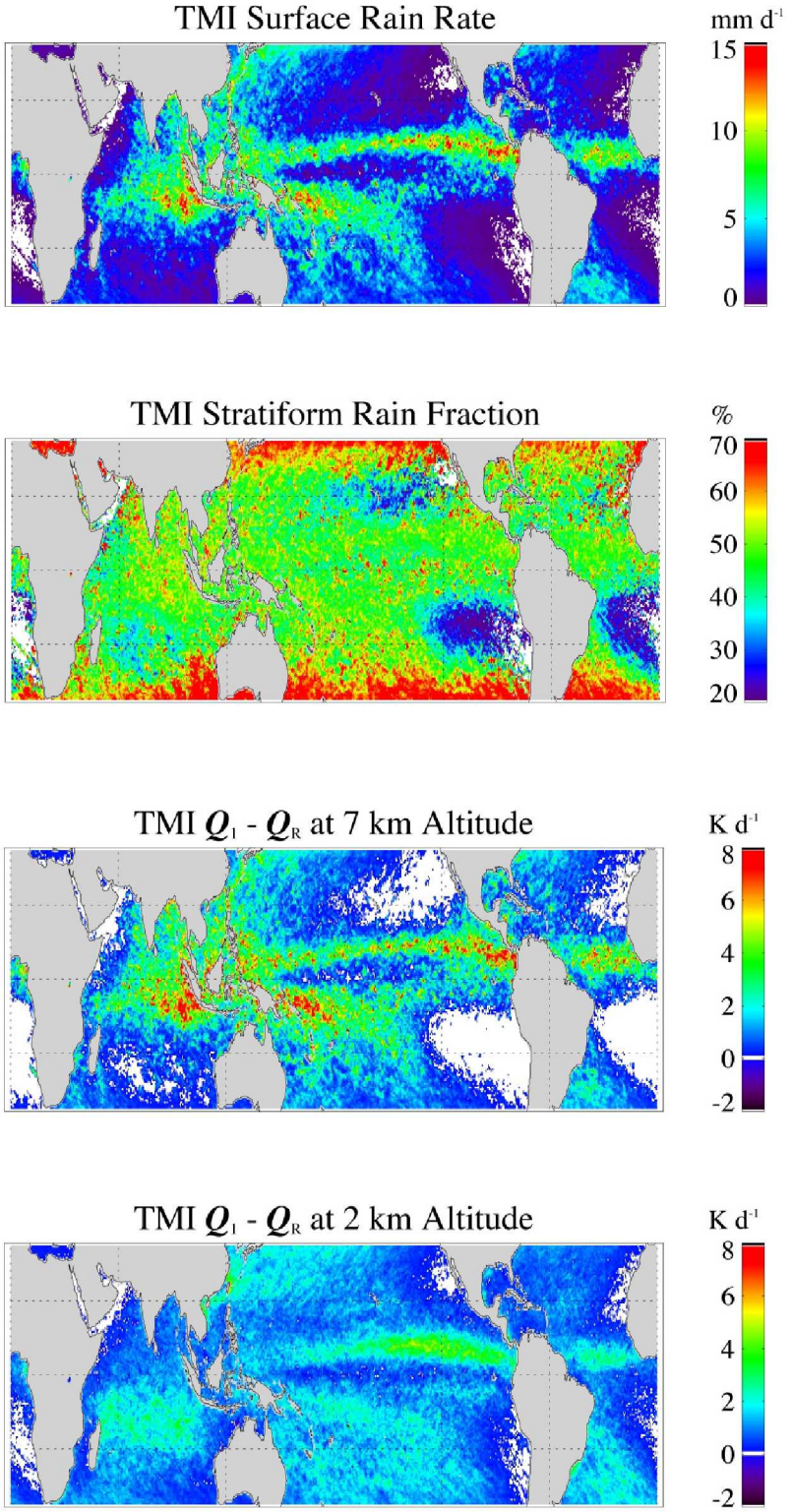

Fig. 3(b)

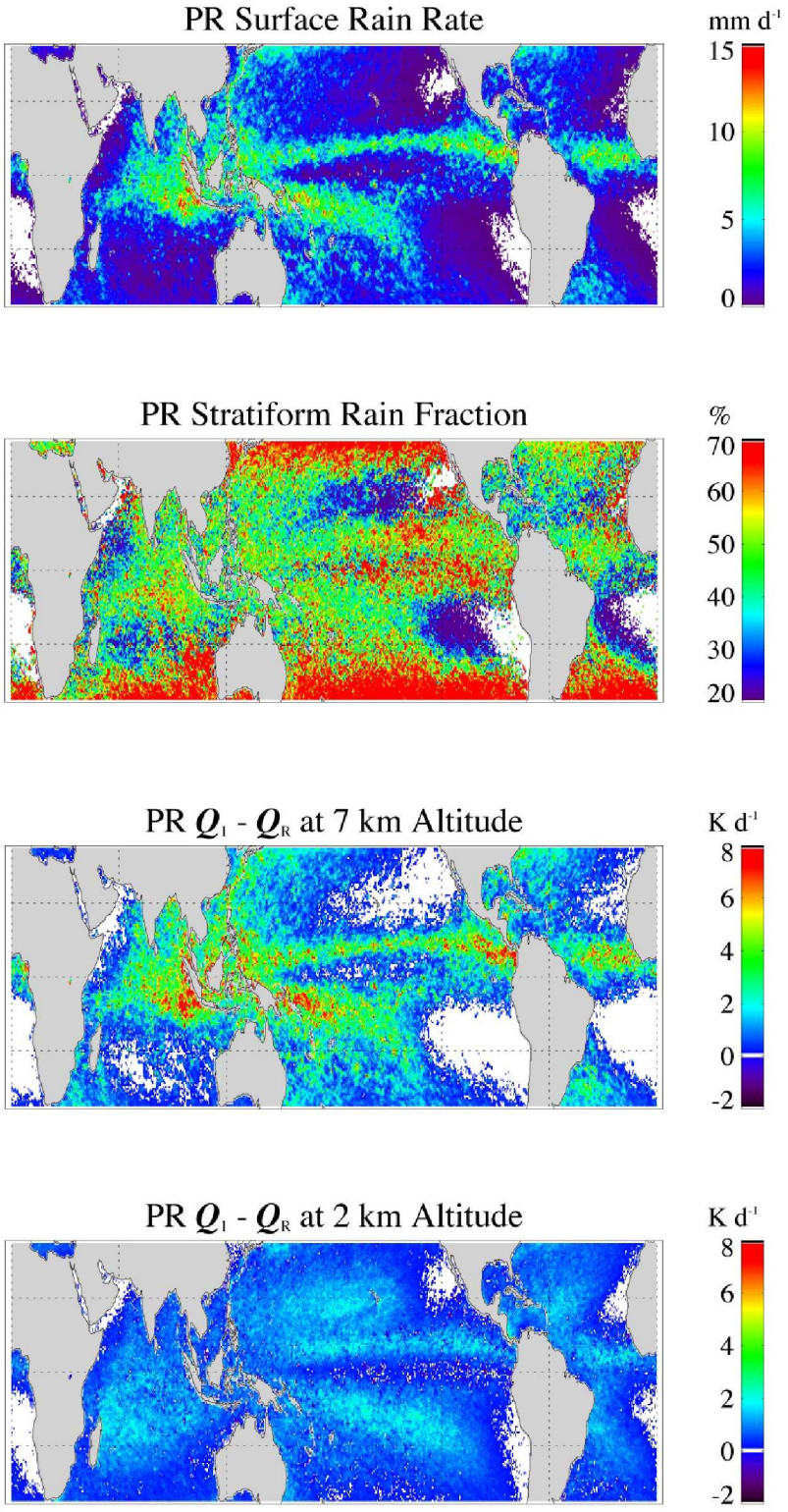
PR Surface Rain Rate
mm d-1
15
10
5
0
PR Stratiform Rain Fraction
%
70
60
50
40
30
20
PR Q_I - Q_R at 7 km Altitude
K d-1
8
6
4
2
0
-2
PR Q_I - Q_R at 2 km Altitude
K d-1
8
6
4
2
0
-2

Fig. 4. Profiles of the mean, standard deviation, bias, and error standard deviation of TMI monthly-mean estimates of Q_I-Q_R for the six regions defined in Table 1, over the period 1 March 1998 – 28 February 1999. Biases and error standard deviations are based upon the differences of estimates from the TMI algorithm and the PR training algorithm. Estimates from the TMI have been subsetted to include only those coinciding with the PR swath.

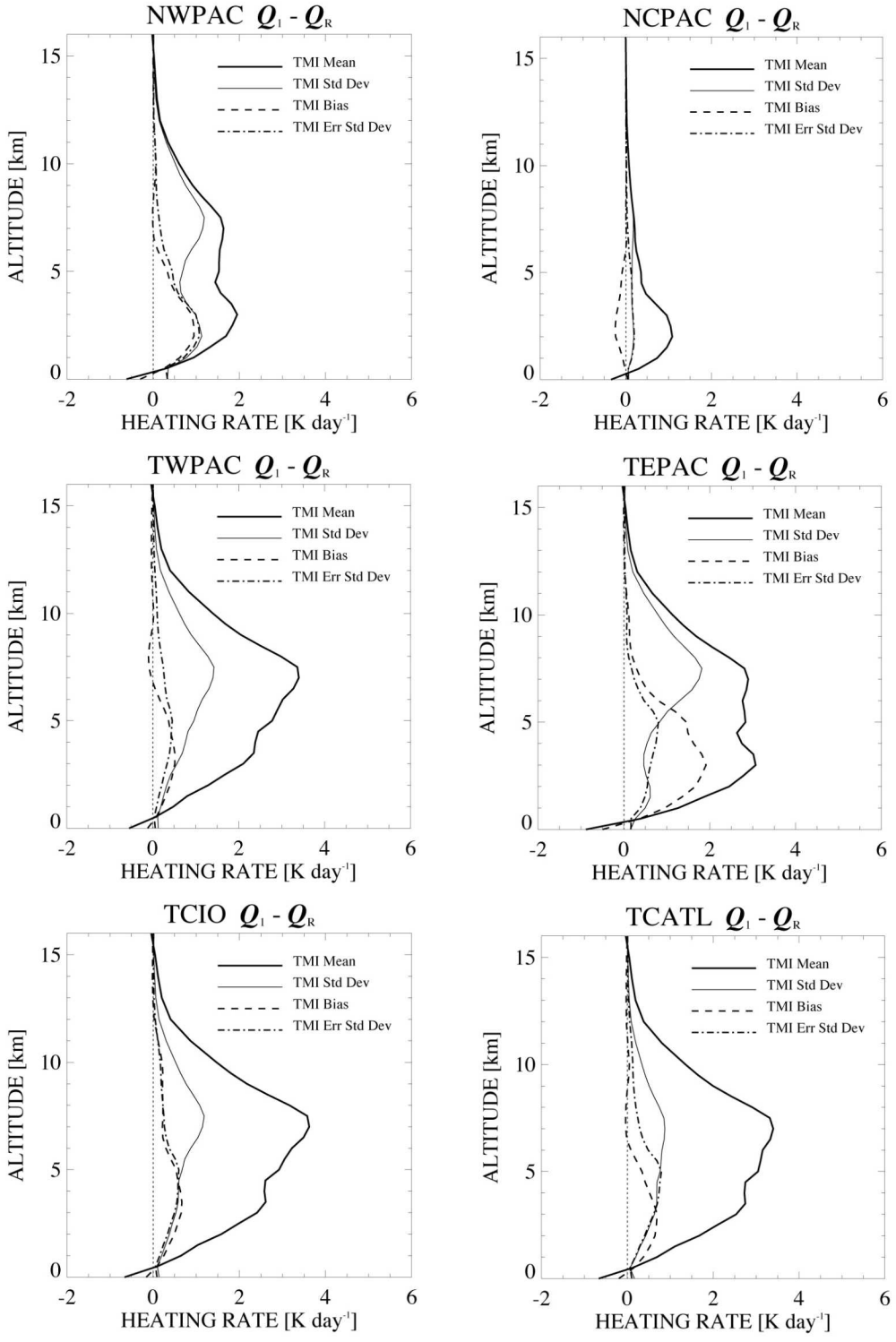

Fig. 5. Same as Fig. 4, but the biases and error standard deviations are estimated potential errors due to the choice of heating lookup table. The biases and error standard deviations are based upon the differences between the TMI algorithm (using the SCSMEX heating lookup table) and an average of TMI algorithm estimates derived using the SCSMEX, TOGA COARE, and KWAJEX heating lookup tables.

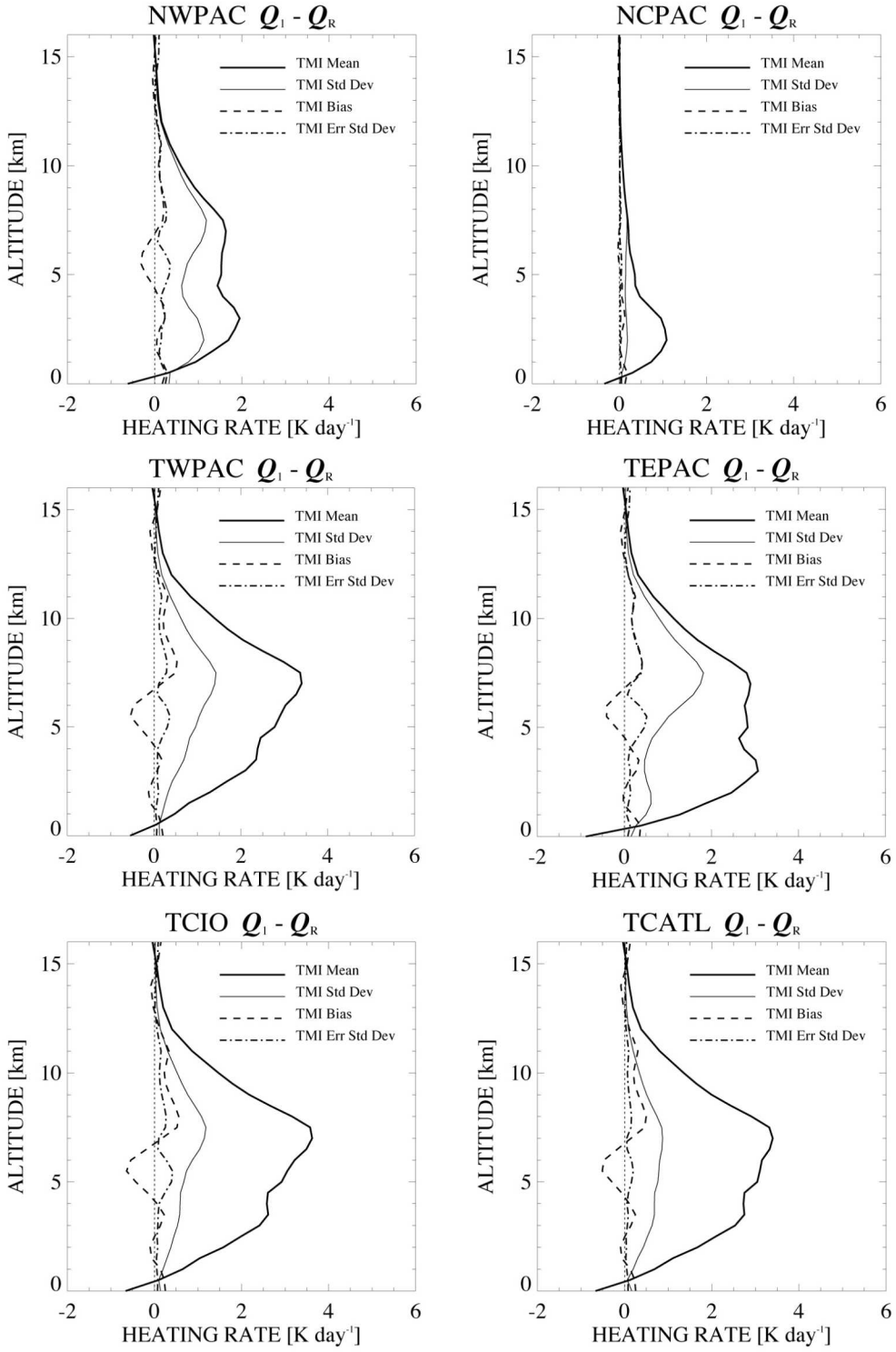

Fig. 6a. Time series of surface rain rates from the TMI algorithm and the rawinsonde moisture budget (top panel), TMI estimates of Q_1-Q_R (second from top), TMI/VIRS combined estimates of Q_1 (third from top), and rawinsonde analyses of Q_1 (bottom panel) for the period 15 May – 20 June, 1998, over the SCSMEX NESA.

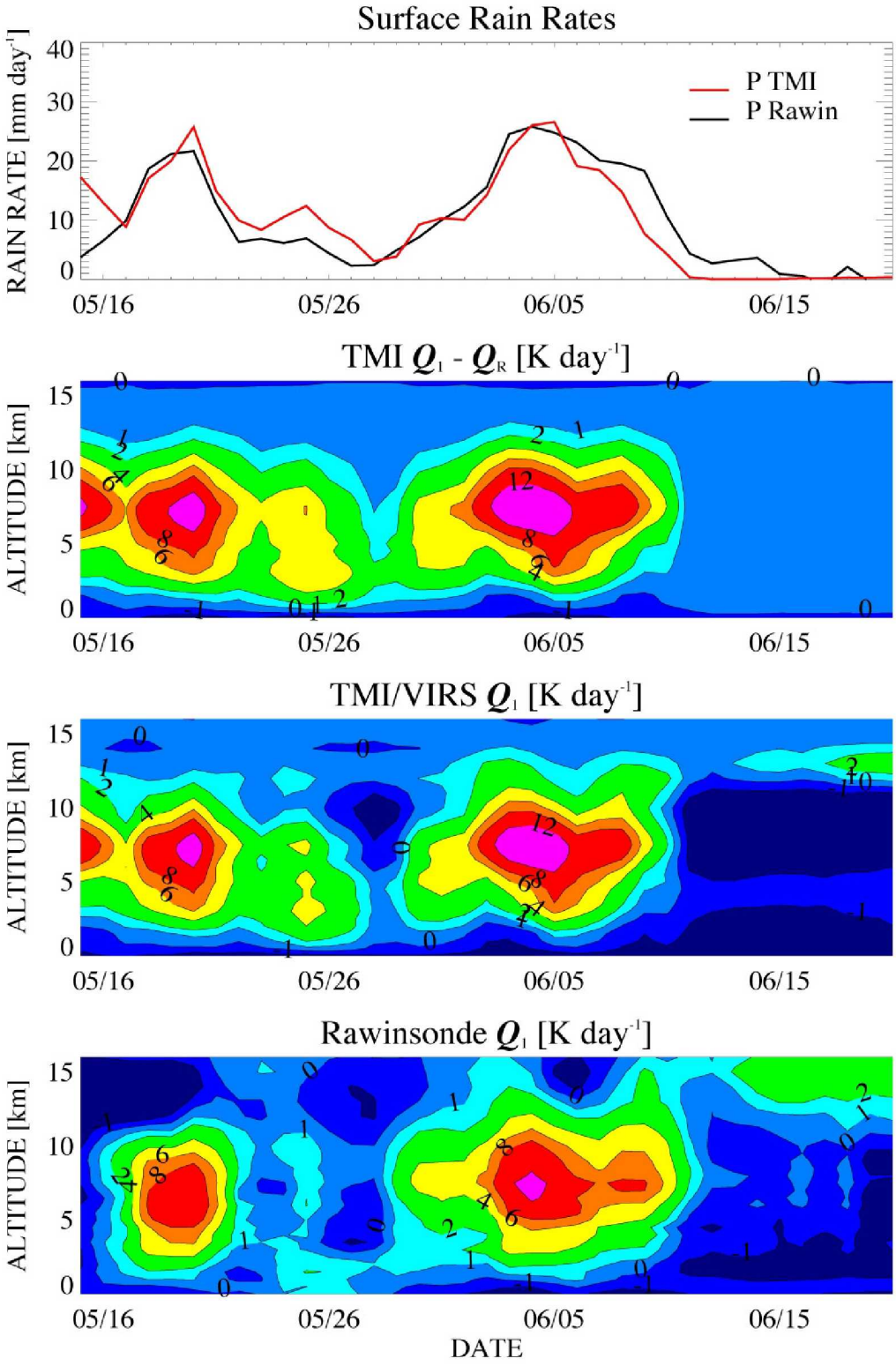

Fig. 6b. Rain rate normalized mean profiles of TMI-estimated Q_1-Q_R, TMI/VIRS combined estimates of Q_1, and rawinsonde analysis estimates of Q_1 for the period 15 May – 20 June, 1998, over the SCSMEX NESA.

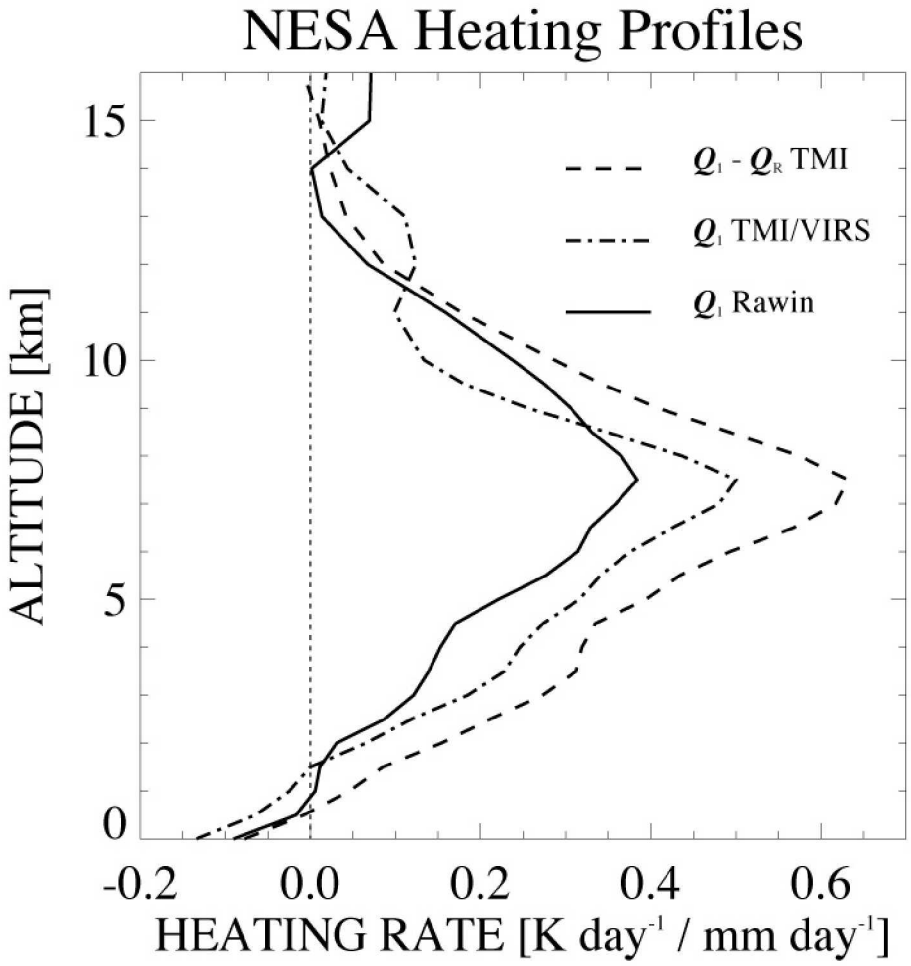

Fig. 7a. Same as Fig. 6a, but for the period 31 October – 26 November, 2006, over the MISMO sounding array.

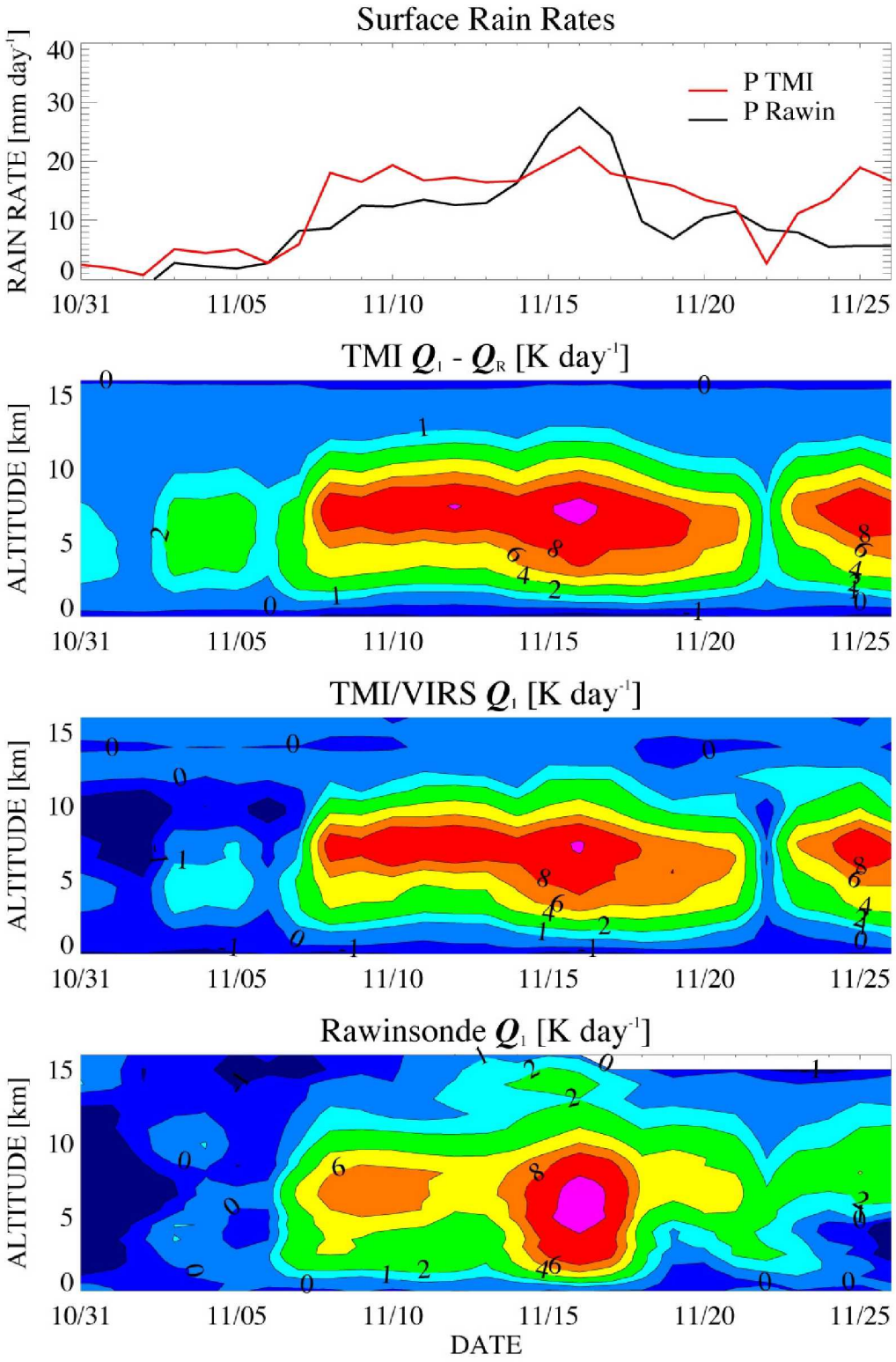

Fig. 7b. Same as Fig. 6b, but for the period 31 October – 26 November, 2006, over the MISMO sounding array.

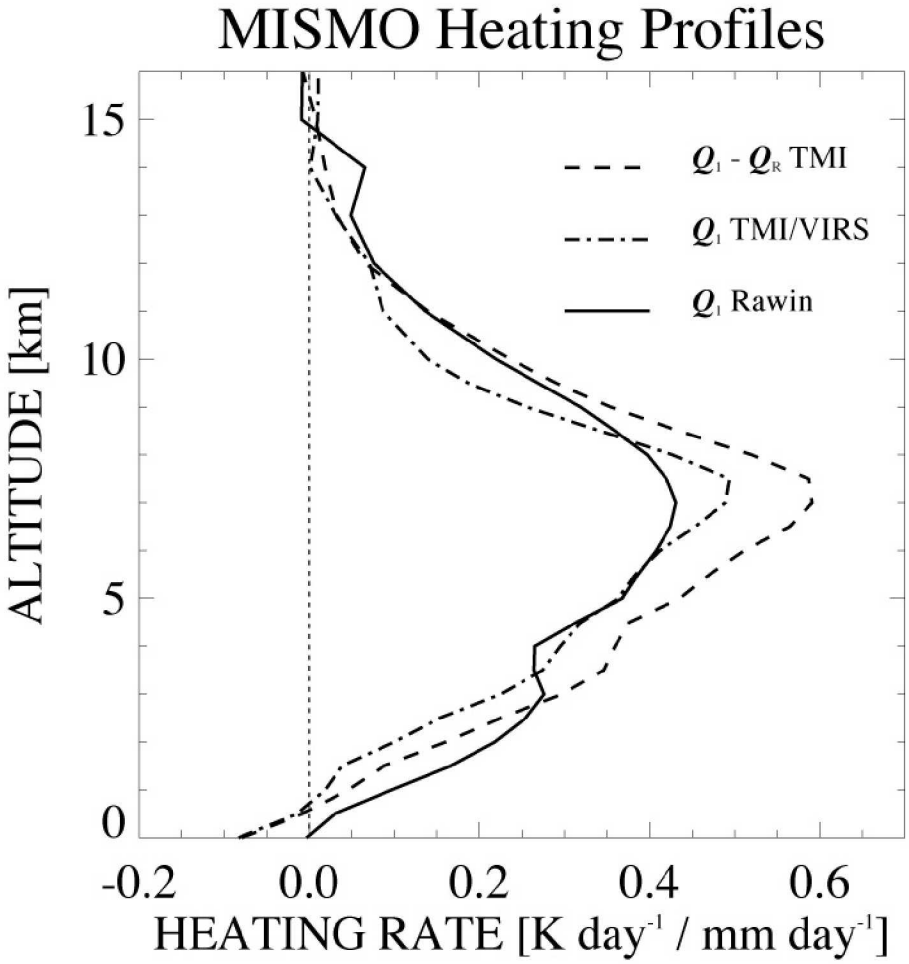

Fig. 8. Estimates of the mean profiles of Q_1-Q_R over the TEPAC region (see Table 1) for the period 1 March 1998 – 28 February 1999, based upon the TMI algorithm and an alternative TMI algorithm (Alt) that utilizes an additional radiance predictor for the local intensity of microwave emission in the 19 GHz horizontal polarization channel.